Int. J. Appl. Math. Comput. Sci., 2020, Vol. 30, No. 3, 449–462
DOI: 10.34768/amcs-2020-0033

MATHEMATICAL METHODS OF SIGNAL ANALYSIS APPLIED IN MEDICAL DIAGNOSTIC

KONRAD A. CIECIERSKI [a]

[a] Bioinformatics and Machine Recognition Department
Research and Academic Computer Network
Kolska 12, 01-045 Warsaw, Poland
e-mail: Konrad.Ciecierski@nask.pl

Digital signal processing, such as filtering, information extraction, and fusion of various results, is currently an integral part of advanced medical therapies. It is especially important in neurosurgery during deep-brain stimulation procedures. In such procedures, the surgical target is accessed using special electrodes while not being directly visible. This requires very precise identification of brain structures in 3D space throughout the surgery. In the case of deep-brain stimulation surgery for Parkinson's disease (PD), the target area—the subthalamic nucleus (STN)—is located deep within the brain. It is also very small (just a few millimetres across), which makes this procedure even more difficult. For this reason, various signals are acquired, filtered, and finally fused, to provide the neurosurgeon with the exact location of the target. These signals come from preoperative medical imaging (such as MRI and CT), and from recordings of brain activity carried out during surgery using special brain-implanted electrodes. Using the method described in this paper, it is possible to construct a decision-support system that, during surgery, analyses signals recorded within the patient's brain and classifies them as recorded within the STN or not. The constructed classifier discriminates signals with a sensitivity of 0.97 and a specificity of 0.96. The described algorithm is currently used for deep-brain stimulation surgeries among PD patients.

Keywords: classification, decision support system, signal filtering, data fusion, temporal analysis.

1. Introduction

Most modern medical procedures cannot be safely performed without technical support. This is particularly observed in medical diagnostic and surgical procedures. Medical imaging techniques, such as computed tomography (CT) and magnetic resonance imaging (MRI) scans, are essential diagnostic tools and are obligatory prerequisites for most advanced surgeries. Both types of scans are possible because of advanced mathematical solutions that recreate cross-sections of the human body from registered x-ray or magnetic data. It is clear that modern medicine cannot advance further without aid from applied mathematics and computer science.

One area in medicine that is very much dependent on computer science is functional neurosurgery. Here, the target of the surgery is often located deep within a patient's brain, and without computerized aid, virtually impossible to localize. In the case of deep-brain stimulation (DBS) surgery for Parkinson's disease (PD), even with the aid of CT and MRI, only an approximate location of the surgical target can be obtained. This is why additional computational aid is required.

Standard DBS surgery for PD is conducted in two steps: (i) using the combined data from CT and MRI scans, a rough localization of the subthalamic nucleus (STN) in the 3D space of a patient's head is determined, and (ii) according to these results, a more precise localization of the STN is obtained using neurosurgical microrecording. The latter is an analysis technique performed by human experts during surgery.

Various mathematical methods of signal analysis can be applied to STN localization with great success rates. These methods, such as wavelet multiresolution analysis, give deeper insights into the data obtained from the microrecordings. This application of advanced mathematics facilitates distinguishing between signals, which – for a person without medical training – could be mistaken for white noise.

The data acquisition is done as follows: using the

3D guidance frame (Schaltenbrand, 1977), an array of three to five parallel microelectrodes is inserted into the patient's brain and directed towards the expected location of the STN. The electrodes are then advanced through the patient's brain. Starting from about 1 cm above the STN, electrodes are advanced in increments of 1 mm. At each step, a simultaneous recording of 10 seconds, on average, is obtained from all electrodes. These steps are repeated until the electrodes pass safely through the STN, and the recordings indicate the presence of another brain structure (the SNr), which is located below the STN (Israel and Burchiel, 2011; Schaltenbrand, 1977).

The distinct hyperactivity of the STN allows an experienced neurosurgeon to distinguish the localization of the STN from other brain regions by simply looking at the microrecording (Levy *et al*., 2000; Parent and Hazrati, 1995; Shamir *et al*., 2012; Hutchison *et al*., 1998; Ciecierski *et al*., 2014b; Mandat *et al*., 2011; Novak *et al*., 2007; Kano *et al*., 2006).

However, there are some difficulties associated with the procedure. The STN is a very small structure (9 $\times$ 4 $\times$ 7 mm) (Israel and Burchiel, 2011; Nieuwenhuys *et al*., 2007) that can only be approximately located using CT and MRI scans. Further, the hyperactivity of the STN (Israel and Burchiel, 2011), which is required for clear interpretation of the microrecordings by an expert, does not always reach levels that provide obvious distinction. The above reasons make this method very subjective, while misdetection of the STN could lead to severe medical complications (Temel *et al*., 2005), including depression, mania, and other severe mood alterations (Mallet *et al*., 2007; Mandat *et al*., 2006; Anderson and Rogers, 2009).

Therefore, it is obvious that the accuracy of STN localization is of highest priority for the surgical treatment of PD symptoms. Further, the duration of the procedure is also crucial, as general anaesthesia cannot be applied owing to its significant effects on brain physiology (Saleh *et al*., 2015; Ho *et al*., 2018).

By applying the author's expert selection of various filters and fusing the results they provide, a novel algorithm has been developed that identifies whether a given signal has been registered within the STN. Classifiers, built according to this algorithm, provide discrimination with a sensitivity of 0.97 and a specificity of 0.96, which is more than satisfactory, even for medical standards (Freeman and Moisen, 2008). The fusion of information obtained from medical imaging, along with the results provided here, can facilitate the creation of an expert decision-support system that provides neurosurgeons with an optimized way to localize the STN.

The computational part of the surgery is conducted as follows: The approximate 3D localization through CT and MRI scans, calculation of the 3D vectors guaranteeing a safe approach to the target within the patient's head, and computerized recording of brain activity in selected areas have been improved substantially. This extension, through computational analysis of brain recordings, facilitates a shorter duration and better precision during surgery.

The rest of the paper is structured as follows. Section 2 provides an overview of related works. Section 3 formulates the goal of the paper, describes input data, and defines discriminative filters. Section 3 also defines the final classifier and algorithms based on it. In Section 4, the classification results are evaluated. Various classification algorithms are run with different subsets of filters. Finally, Section 5 concludes the paper.

2. Related works

The problem of distinguishing recordings acquired within the STN from those acquired in other parts of the brain has been covered in the literature for over ten years. There are various approaches and solutions to this problem. A review of some of the most notable papers related to this subject is provided below:

Moran *et al*. (2006) aim to detect the STN entry and exit points on the track of the electrode using the Bayesian approach on the RMS value of the recorded signal. The obtained error in predicting the STN entry was 0.18 ± 0.84 mm, and the exit point was detected with 0.50 ± 0.59 mm accuracy. However, the paper does not provide any methods for artifact removal. Signals containing artifacts were not used for calculations.

Zaidel *et al*. (2009), in a similar manner to Moran *et al*. (2006), focused on the detection of the STN entry and exit points on the track of the electrode. This paper also focused on the RMS of the signal, but instead of the Bayesian approach, it used the hidden-Markov model. The described method removes only artifacts introduced by the power supply. It is not specified how signals with artifacts from another origin were treated. The obtained results are similar to those found by Moran *et al*. (2006).

Cagnan *et al*. (2011) focused on the detection of the STN based on the signal's power in frequency bands below 100 Hz. Artifact removal was based only on an amplitude threshold. The overall accuracy of the method with surgical protocols is 88%. Neither sensitivity nor specificity is provided.

Schiaffino *et al*. (2016) distinguished STN recordings using the K-NN classifier, which is based upon eight spike-independent and seven spike-dependent features. Recordings containing artifacts were discarded by authors, who obtained a sensitivity of 0.86, and a specificity of 0.90.

Valsky *et al*. (2017) focused on the detection of the point where the electrode exits the STN. Based on the RMS and the signal power in frequency bands below 300 Hz, discrimination is done using the SVM classifier and

a hidden-Markov model. As the method focuses only on the detection of the bottom border of the STN, it provides neither sensitivity nor specificity. The bottom border of the STN is detected with an error of 0.04 ± 0.18 mm.

Some of the reviewed papers focus solely on the detection of one or both of the STN borders, while others attempt to classify all available recordings. In most cases, the detection is based on spike activity or on the power of the signal at frequencies below 500 Hz. No paper focuses on frequencies above 500 Hz. Artifacts that are ever-present in neurobiological recordings are not filtered out or are filtered based upon the amplitude only. In many cases, all signals with artifacts are discarded.

3. Problem formulation

The goal of this paper is to construct an algorithm that, for a given input signal registered by electrode e at depth d, provides information on whether this signal has been acquired within the STN.

Definition 1. (*Depth sets*) Let the set of depths in μm, be defined as

$$D = \{-10000, -9000, \ldots, 0, \ldots, d_E\} \tag{1}$$

where $d_E \leq 6000$ and, $\forall d \in D,\ d \mod 1000 = 0$. Let the base set of depths, in μm be defined as

$$D_B = \{-10000, \ldots, -6000\} \tag{2}$$

where $D_B \subset D$.

Definition 2. (*Input signal*) Let the input signal registered by electrode e at depth $d \in D$ be defined as

$$\text{mer}(e, d) = (x_{e,d,1}, \ldots, x_{e,d,n_{e,d}}), \tag{3}$$

where $n_{e,d}$ is the number of recorded samples.

Definition 3. (*Filter*) For input signal $\text{mer}(e, d)$, define a function f, such that $f(\text{mer}(e, d)) \in \mathbb{R}$ is a defined filter

$$F(f, e, d) = f(\text{mer}(e, d)), \tag{4}$$

Assuming that

$$f_B(e) = \operatorname*{avg}_{d \in D_B} f(\text{mer}(e, d)), \tag{5}$$

the normalized filter is defined as

$$F_N(f, e, d) = \frac{f(\text{mer}(e, d))}{f_B(e)}. \tag{6}$$

Definition 4. (*Binary classifier*) For signal $\text{mer}(e, d)$ and a set of filters $\text{FS} = \{F_1, \ldots, F_i, F_{N_1}, \ldots, F_{N_j}\}$ define a binary classifier

$$\text{BC}(\text{FS}, \text{mer}(e, d)) = \begin{cases} 1 & \text{if mer}(e, d) \text{ acquired} \\ & \text{within the STN,} \\ 0 & \text{otherwise.} \end{cases} \tag{7}$$

3.1. Input data. In most cases, in each hemisphere, the recording begins at depth –10000 μm (i.e., 10 mm above the estimated STN location) and continues in increments of 1000 μm, up to a depth of $+6000$ μm (see Definition 1). Each recording (see Definition 2) made by a given electrode at each location is at least 10 s long and is sampled at 24 kHz. For the purpose of recording, three to five electrodes are typically used. The datasets used in this paper are obtained from 50 surgeries, and contain 6540 recordings, averaging to 131 recordings per patient. Of those 6540 recordings, 5422 recordings (83%) were according to neurosurgical protocols labelled as recorded outside of the STN, while 1118 (17%) were labelled as recorded within the STN.

3.2. Definition of filters. As filters are the basis upon which a classifier makes its decisions, they are of utmost importance in this algorithm. Filters must be constructed in such a way that their values would significantly differ for recordings made within the STN and outside of it.

Discrete neuron activity-based filters. The electrical activity of a neuron is registered by an electrode as a voltage spike. Typically, in the STN, they are below 200 μV (Israel and Burchiel, 2011). Registered spikes are discrete events in time and can be additionally sorted according to their shape. As the shape of the spike is dependent on the cell structure (Nieuwenhuys *et al.*, 2007; Lewicki, 1998; Koch, 2004), it remains unchanged in a given recording. Therefore, it is clear that spikes of different shapes must originate from different neuron cells. Two most obvious characteristics are the average number of spikes per second and the bursting ratio. The bursting ratio is based upon the lengths of intervals between consecutive spikes and is defined here as the fraction of intra-spike intervals that are not longer than 33 ms.

Definition 5. (*Spike activity-based filters*) Assuming that $f_1(\text{mer}(e, d))$ is the average number of spikes per second in $\text{mer}(e, d)$ (see Definition 2), AvgSpkRate denotes $F(f_1, e, d)$ (see Definition 3). For $f_2(\text{mer}(e, d))$, representing the maximum average number of spikes per second obtained from a single cell in $\text{mer}(e, d)$ (see Definition 2), AvgSpkRateScMax denotes $F(f_2, e, d)$ (see Definition 3). For $f_3(\text{mer}(e, d))$, representing the fraction of intra-spike intervals that are no longer than 33 ms observed in $\text{mer}(e, d)$ (see Definition 2), BurstRatio denotes $F(f_3, e, d)$ (see Definition 3). Finally, assuming that $f_4(\text{mer}(e, d))$ is the fraction of intra-spike intervals generated by a single cell that are no longer than 33 ms and are observed in a given $\text{mer}(e, d)$ (see Definition 2), BurstRatioScMax denotes $F(f_4, e, d)$ (see Definition 3).

Construction of spike activity-based filters is explained in detail in a study by Ciecierski *et al.* (2014b).

The wavelet transform provides a mathematical framework that can be applied in many areas of digital processing for medical data. The model of signal processing provided by the wavelet transform facilitates a shift in signal analysis from the time–amplitude to the time–frequency plane (Jensen and la Cour-Harbo, 2001). This allows analysis of the original signal in various frequency domains while still retaining the temporal information from the original signal. When a certain feature is detected in the time–frequency plane, its time of occurrence in the original signal is readily available. The wavelet transform is always based upon the set of mother-wavelet functions. Their choice can be of significant importance and depends on the original data. For some data, simple Haar functions are sufficient, while for other datasets, different functions are proven to obtain better results. In the case of neurological signals, the Daubechies D4 wavelet is commonly used. In this paper, all wavelet transformations are D4-based. Finally, as the wavelet transform is reversible, it is possible to switch to the time-frequency plane, make the required adjustments in the frequency domain, and return to the time–amplitude plane. Such operations constitute the base model for the filtering of a signal in the frequency domain. This model is used in the paper as the core feature, as it is the basis for the removal of artifacts, as well as for the calculation of some essential filters.

Definition 6. (*Discrete wavelet decomposition forwards step*) The signal S_k containing $2n$ samples and reflecting frequencies below f Hz is decomposed into two signals, each containing n samples: S_{k+1} (containing n samples and reflecting S_k in frequencies below $f/2$ Hz) and D_{k+1} (containing n samples and reflecting S_k in frequencies between $f/2$ Hz and f Hz). Such octave-based decomposition, while being commonly used, is only a particular case of wavelet analysis. Other versions of wavelet analysis with different filter banks do exist.

The above implies that any signal that can be fully decomposed using the wavelet transform has to have a number of samples that is a power of 2. The signal with a number of samples 2^n can be maximally decomposed in n steps, resulting in final S and D being singleton sets.

Definition 7. (*Discrete wavelet decomposition*) Assume that the original signal S_0 is sampled with frequency f_0 Hz, and has n samples (n being a power of 2). Then, for $k = 1, \ldots, \log_2 n$, denote by S_k the tuple of $n/2^k$ wavelet coefficients representing the signal S_0 in frequencies $(0, f_0/2^{k+1}]$ and by D_k the tuple of $n/2^k$ wavelet coefficients representing the signal S_0 in frequencies $(f_0/2^{k+1}, f_0/2^k]$. The full decomposition is therefore represented as the set

$$\mathrm{WD}(S_0, f_0) = \{S_{\log_2 n}, D_{\log_2 n}, \ldots, D_1\}. \tag{8}$$

Definition 8. (*Frequency mapping*) For the original signal sampled with frequency f_0 Hz, the frequency coverage the tuple S_k can be defined as $FC_S(f_0, k) = (0, f_0/2^{k+1}]$ while the frequency coverage the tuple D_k can be defined as $FC_D(f_0, k) = (f_0/2^{k+1}, f_0/2^k]$. Finally, for the original signal S_0 sampled with frequency f_0 Hz, and for a given continuous, left open, frequency interval $\mathbb{F}$, a defined function returning a set of tuples of wavelet coefficients that fit into its range can be created.

$$\begin{aligned}&\mathrm{FC}(S_0, f_0, \mathbb{F})\\ &= \{S_k \in \mathrm{WD}(S_0, f_0) : k = \log_2 n \wedge \mathrm{FC}_S(f_0, k) \subseteq \mathbb{F}\}\\ &\qquad\cup\\ &\{D_k \in \mathrm{WD}(S_0, f_0) : k \leq \log_2 n \wedge \mathrm{FC}_D(f_0, k) \subseteq \mathbb{F}\}.\end{aligned} \tag{9}$$

Definition 9. (*Artifact filtering*) For a given signal $(x_1, \ldots, x_n)$ and threshold t the thresholding function can be defined as $(y_1, \ldots, y_n) = \mathrm{thr}((x_1, \ldots, x_n), t)$, where

$$y_i = \begin{cases} x_i & \text{if } |x_i| \leq t,\\ 0 & \text{otherwise.}\end{cases} \tag{10}$$

For a given signal $mer(e, d)$ sampled with 24 kHz and right-padded to its length being a power of 2, the partial-wavelet decomposition can be defined as

$$\mathrm{WD}_5(\mathrm{mer}(e, d)) = (S_5, D_5, D_4, D_3, D_2, D_1). \tag{11}$$

Using the function

$$t_{5N}(x) = \mathrm{thr}(x, 5\sigma_N(x)), \tag{12}$$

we get

$$\begin{aligned}\mathrm{WDT}_5 = (&t_{5N}(S_5), t_{5N}(D_5), t_{5N}(D_4), t_{5N}(D_3),\\ &t_{5N}(D_2), t_{5N}(D_1)).\end{aligned} \tag{13}$$

As sets S and D represent the original signal in various frequency bands, the function t_{5N} acts in the frequency domain. From WDT_5, by means of the inverse-wavelet transform, the filtered $\mathrm{mer}(e, d)$ can be obtained and defined as $\mathrm{artrem}(\mathrm{mer}(e, d))$. In the above definition, the following estimation of standard deviation is used

$$\sigma_N = \frac{1}{0.6745}\mathrm{median}(|x_1|, \ldots, |x_n|). \tag{14}$$

Filters based on the background activity. The amplitude of the electrical activity in neural tissue is low. In the STN and adjacent areas, the observed spikes do not exceed 200 μV, and the background activity is below 50 μV (Israel and Burchiel, 2011). This implies that, during the recording process, the signal needs to be greatly amplified. This makes the signal very prone to contamination by artifacts generated from non-neural sources. These sources include the heartbeat, the frequency of the main power supply, or the noise present in the operation theatre. Any mechanical contact, such as a slight nudge to the 3D frame that holds the patient's head, also produces significant artifacts in the recordings.

It has been found that, without a good methodology designed for the removal of these artifacts, filters calculated from the background activity are so strongly distorted that their values are almost random and provide very little useful information (Ciecierski *et al*., 2014a). This is a well-known problem in this field of research (see Section 2), and in many cases, recordings with such contamination are left unchanged, filtered by an amplitude threshold (Cagnan *et al*., 2011), or even simply discarded (Schiaffino *et al*., 2016). Here, as the system was developed as a practical aid during neurosurgical procedures, discarding the data was not an option, and a completely new dedicated artifact-removal procedure has been developed (see Definition 9). The degree of wavelet decomposition and levels of thresholding are wholly the author's own intellectual creation. The novelty of this method is applying the thresholding and filtering in the frequency domain rather than the amplitude domain. The effectiveness of artifact removal can be seen in Fig. 1.

Filters calculated from the background activity are always calculated in the context of a pass of the given electrode. This is because of the normalization process (see Definition 3), which is made using a baseline level calculated from the first five millimetres of the recording pass (see Definition 1). As the recording starts at a certain distance from the expected location of the STN, and the electrode approaches the STN from above, the first recorded depths are expected to be within a part of the brain with lower activity (Nieuwenhuys *et al*., 2007). This activity is low, especially in comparison with the STN activity (Israel and Burchiel, 2011), and can be so used as a reference point – the baseline level f_B of a filter (see Definition 3).

It becomes clear that, if any of the background activity-based filters described below has a value ν, this implies that it is ν times as large as its non-normalized average calculated for the base depths D_B (see Definition 1).

Definition 10. (*Background activity-based filters*) Assuming that $\mathrm{mer}(e,d)$ is a recording sampled with frequency 24000 Hz, the following functions can be defined:

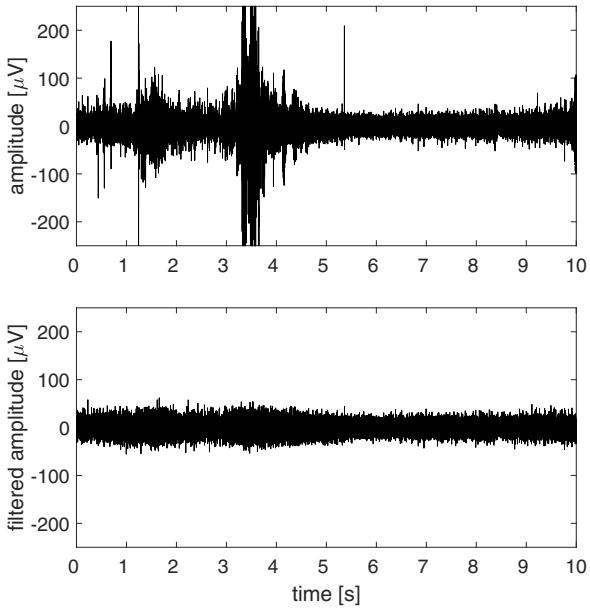

Fig. 1. Recording before and after artifact removal.

$$f_{\mathrm{PRC80}}(\mathrm{mer}(e,d)) = P_{80\%}(|\mathrm{artrem}(\mathrm{mer}_{e,d})|) \tag{15}$$

as the 80th percentile of the absolute value of the filtered amplitude of $\mathrm{mer}(e,d)$,

$$f_{\mathrm{RMS}}(\mathrm{mer}(e,d)) = \sqrt{\frac{1}{n_{e,d}} \sum_{x \in \mathrm{artrem}(\mathrm{mer}(e,d))} x^2} \tag{16}$$

as the RMS value of filtered $\mathrm{mer}(e,d)$.

Having

$$\mathrm{PWR}(\mathrm{mer}_{e,d}, f_0, f_b, f_e) = \sum_{T \in \mathrm{FC}(\mathrm{mer}_{e,d}, f_0, (f_b, f_e])} \sum_{x \in T} x^2 \tag{17}$$

as the power of the signal sampled with frequency f_0 in the frequency band spanning from f_b to f_e, one can define

$$f_{\mathrm{LFB}}(\mathrm{mer}(e,d)) = \mathrm{PWR}(\mathrm{artrem}(\mathrm{mer}_{e,d}), 24000, 0, 500) \tag{18}$$

as the power of the signal $\mathrm{mer}(e,d)$ in frequencies below 500 Hz.

$$f_{\mathrm{HFB}}(\mathrm{mer}(e,d)) = \mathrm{PWR}(\mathrm{artrem}(\mathrm{mer}_{e,d}), 24000, 500, 3000) \tag{19}$$

as the power of the signal $\mathrm{mer}(e,d)$ in frequencies between 500 Hz and 3 kHz.

Using the function defined above, the following background-activity based filters are defined:

$$\text{PRC80}(e,d) = F_N(f_{\text{PRC80}}, e, d), \tag{20}$$

$$\text{RMS}(e,d) = F_N(f_{\text{RMS}}, e, d), \tag{21}$$

$$\text{LFB}(e,d) = F_N(f_{\text{LFB}}, e, d), \tag{22}$$

$$\text{HFB}(e,d) = F_N(f_{\text{HFB}}, e, d). \tag{23}$$

Let also

$$\text{BAS} = \{\text{PRC80}, \text{RMS}, \text{LFB}, \text{HFB}\}. \tag{24}$$

Filters based on the moving average. For each of the background activity-based filters (PRC80, RMS, LFB, and HFB), the moving average (Smith, 1997) is calculated. In this manner, other four filters are defined: MPRC80, MRMS, MLFB, and MHFB.

Definition 11. (*Moving average-based filters*) Let the padded form of filter $F(e,d) \in \text{BAS}$ be defined as

$$\text{PAD}_1(F(e,d)) = \begin{cases} F(e,d) & \text{if } d \in D, \\ 1 & \text{otherwise.} \end{cases} \tag{25}$$

Using the filters from Definition 10, the following filters are defined:

$$\text{MPRC80}(e,d) = \frac{1}{5}\sum_{k=-2}^{2} \text{PAD}_1(\text{PRC80}(e, d+1000k)), \tag{26}$$

$$\text{MRMS}(e,d) = \frac{1}{5}\sum_{k=-2}^{2} \text{PAD}_1(\text{RMS}(e, d+1000k)), \tag{27}$$

$$\text{MLFB}(e,d) = \frac{1}{5}\sum_{k=-2}^{2} \text{PAD}_1(\text{LFB}(e, d+1000k)), \tag{28}$$

$$\text{MHFB}(e,d) = \frac{1}{5}\sum_{k=-2}^{2} \text{PAD}_1(\text{HFB}(e, d+1000k). \tag{29}$$

The above filters are the five-element wide moving averages of the filters described in Definition 10.

Temporal filters. The temporal filters reflect maximal—encountered on the track of the given electrode—positive or negative changes in the values of filters that are based upon the background activity. The changes are monitored by comparing the current depth with those 1000 μm and 2000 μm above it. For a given electrode e, depth d, and $F \in \text{BAS}$ (see Definition 11), $F(e,d)$ denotes the value of filter F calculated for the recording registered by the electrode e at depth d. For $F \in \text{BAS}$, the following can be defined.

Definition 12. (*Filter delta*) For $F \in \text{BAS}$ define

$$\text{dlt}(F,e,d,\text{step}) = \begin{cases} 0 & \text{if } d < \min(D), \\ F(e,d) - F(e,d-\text{step}) & \text{otherwise.} \end{cases} \tag{30}$$

Now, using filter delta 'dlt' it is possible to define the temporal filters:

Definition 13. (*Temporal filters*) For $F \in \text{BAS}$ the following can be defined:

$$\text{dlt}_{\text{MAX}}(F,e,d,k) = \max_{d_i \le d} \text{dlt}(F,e,d_i,k), \tag{31}$$

$$\text{dlt}_{\text{MIN}}(F,e,d,k) = \min_{d_i \le d} \text{dlt}(F,e,d_i,k) \tag{32}$$

as maximal positive and negative changes in the value of F. For $F \in \text{BAS}$, one can define the following filters:

$$\begin{aligned} \text{DU1}(F(e,d)) &= \text{dlt}_{\text{MAX}}(F,e,d,1000), \\ \text{DU2}(F(e,d)) &= \text{dlt}_{\text{MAX}}(F,e,d,2000), \\ \text{DD1}(F(e,d)) &= \text{dlt}_{\text{MIN}}(F,e,d,1000), \\ \text{DD2}(F(e,d)) &= \text{dlt}_{\text{MIN}}(F,e,d,2000). \end{aligned} \tag{33}$$

From this, 16 temporal filters can be defined as follows:

$$\begin{aligned} \text{DU1\_PRC80}(e,d) &= \text{DU1}(\text{PRC80}(e,d)), \\ \text{DU2\_PRC80}(e,d) &= \text{DU2}(\text{PRC80}(e,d)), \\ \text{DD1\_PRC80}(e,d) &= \text{DD1}(\text{PRC80}(e,d)), \\ \text{DD2\_PRC80}(e,d) &= \text{DD2}(\text{PRC80}(e,d)), \\ \text{DU1\_RMS}(e,d) &= \text{DU1}(\text{RMS}(e,d)), \\ \text{DU2\_RMS}(e,d) &= \text{DU2}(\text{RMS}(e,d)), \\ \text{DD1\_RMS}(e,d) &= \text{DD1}(\text{RMS}(e,d)), \\ \text{DD2\_RMS}(e,d) &= \text{DD2}(\text{RMS}(e,d)), \\ \text{DU1\_LFB}(e,d) &= \text{DU1}(\text{LFB}(e,d)), \\ \text{DU2\_LFB}(e,d) &= \text{DU2}(\text{LFB}(e,d)), \\ \text{DD1\_LFB}(e,d) &= \text{DD1}(\text{LFB}(e,d)), \\ \text{DD2\_LFB}(e,d) &= \text{DD2}(\text{LFB}(e,d)), \\ \text{DU1\_HFB}(e,d) &= \text{DU1}(\text{HFB}(e,d)), \\ \text{DU2\_HFB}(e,d) &= \text{DU2}(\text{HFB}(e,d)), \\ \text{DD1\_HFB}(e,d) &= \text{DD1}(\text{HFB}(e,d)), \\ \text{DD2\_HFB}(e,d) &= \text{DD2}(\text{HFB}(e,d)). \end{aligned} \tag{34}$$

The temporal filters are designed in such a way as to latch onto an increase or decrease in the values of the filters based on the background activity in the context of a pass of a given electrode. Assuming that a certain filter F has an increased value for the recordings made within the

STN, DU1$(F_N(e,d))$ and DU2$(F_N(e,d))$ will have an increased value in the STN, and at depths below it, those filters change values on the top border of the STN. When considered alone, these filters discriminate data recorded at depths above the STN but fail to distinguish the STN from structures located below it.

DD1$(F_N(e,d))$ and DD2$(F_N(e,d))$ will have decreased values at depths below the STN; those filters change values at the bottom border of the STN. When considered alone, these filters discriminate data recorded at depths below the STN but fail to distinguish the STN from structures located above it.

Filter summary. In Section 3, 28 filters are defined:

- Four spike activity-based filters: AvgSpkRate, the average number of spikes per second in a given recording; AvgSpkRateScMax, the maximal AvgSpkRate obtained from a single neuron; BurstRatio, the fraction of the intra-spike intervals that are no longer than 33 ms; BurstRatioScMax, maximal BurstRatio obtained from a single neuron.

- Four background activity-based filters: PRC80, normalized 80-th percentile of a recording's amplitude absolute value; RMS, normalized root mean square of the recording; LFB, normalized power of the recording in a band below 500 Hz; HFB, normalized power of the recording in the band between 500 Hz and 3 kHz.

- Four moving average-based filters: MPRC80, MRMS, MLFB, MHFB.

- Sixteen temporal filters: DU1_PRC80, DU2_PRC80, DD1_PRC80, DD2_PRC80, DU1_RMS, DU2_RMS, DD1_RMS, DD2_RMS, DU1_LFB, DU2_LFB, DD1_LFB, DD2_LFB, DU1_HFB, DU2_HFB, DD1_HFB, DD2_HFB.

To simplify the notation further, the following sets of filters are defined.

Definition 14. (*Sets of filters*)

$$\begin{aligned}
\text{SA} &= \{\text{AvgSpkRate, AvgSpkRateScMax,} \\
&\quad \text{BurstRatio, BurstRatioScMax}\}, \\
\text{BA} &= \{\text{RMS, PRC80, LFB, HFB}\}, \\
\text{MA} &= \{\text{MRMS, MPRC80, MLFB, MHFB}\}, \\
\text{DU1} &= \{\text{DU1_PRC80, DU1_RMS,} \\
&\quad \text{DU1_LFB, DU1_HFB}\}, \\
\text{DU2} &= \{\text{DU2_PRC80, DU2_RMS,} \\
&\quad \text{DU2_LFB, DU2_HFB}\}, \\
\text{DD1} &= \{\text{DD1_PRC80, DD1_RMS,} \\
&\quad \text{DD1_LFB, DD1_HFB}\}, \\
\text{DD2} &= \{\text{DD2_PRC80, DD2_RMS,} \\
&\quad \text{DD2_LFB, DD2_HFB}\}, \\
\text{DALL} &= \text{DU1} \cup \text{DU2} \cup \text{DD1} \cup \text{DD2}, \\
\text{ALL} &= \text{SA} \cup \text{BA} \cup \text{MA} \cup \text{DALL}.
\end{aligned} \tag{35}$$

3.3. Binary classifier. For classifying recordings based on defined filters (see Definition 4), the AdaBoost classifier has been selected (Dietterich, 2000). As this classifier is particularly well suited to imbalanced data (83% of the recordings used in calculations here were originally labeled as recorded outside the STN), it is the most obvious first choice. AdaBoost is an ensemble classifier that makes decisions based on the weighted sum of decisions of tree-based weak learners. In the process of training, the weights are modified to minimize the error in the training set. All results given below have been obtained using a Matlab implementation (AdaBoostM1) and ten-fold cross-validation. Additionally, in Section 4.3, the results obtained using AdaBoost are compared with those obtained using an SVM classifier with different kernels (Williams, 2003). The original class of each recording is set according to the information taken from the neurosurgical protocol. This information has been filled by the neurosurgeon during the DBS procedure.

3.4. Algorithm. The algorithm for decision making during the DBS procedure is Algorithm 1. During Step 7 the values of the selected filters are calculated for all of the recordings acquired during Step 5. The classification process is then made in Step 8. The detailed actions performed during Steps 7 and 8 are described in Algorithm 2. Step 9 is the crucial point of the combination of digital signal processing, filtering, and classification provides neurosurgeons with the diagnostic information.

4. Performance evaluation

Two approaches to the classification problem were tested using the AdaBoost classifier. The author set the AdaBoost parameters to the following values:

- the number of trees in the ensemble: 500,
- the minimal tree leaf size: 5,
- the learning rate: 0.1.

Both the approaches were focused on the selection of an optimal set of filters that would give results comparable to those achieved using a set of all 28 filters. The first approach is a novel one based upon the author's own

Algorithm 1. Decision making during DBS surgery.

Step 1. Using medical imaging, acquire CT and MRI data.

Step 2. Fusing the data from CT and MRI, the surgeon obtains an approximate location of the STN.

Step 3. Surgery begins.

Step 4. An array of 3 to 5 electrodes are advanced towards the STN to a point roughly 10 mm above its center.

Step 5. For a span of 16 mm, moving in 1 mm increments, electrodes record brain activity.

Step 6. Artifacts present in recorded data are removed using a novel, wavelet-based filter.

Step 7. The set of filters devised, tested, and developed by the author are calculated for each of the acquired recordings. Typically, during surgery, around 100 recordings are classified (see Algorithm 2).

Step 8. Using the information fusion provided by the filters, the classifier assesses which recordings were made within the STN.

Step 9. Using the information fusion provided by the classifier, the extent of the STN on the track of each electrode is obtained. In this way, the computational solution provides neurosurgeons with the locations of the upper and lower borders of the STN within the patient's brain.

Step 10. Neurosurgeons use data acquired during surgery, along with the localization provided by the classifier, to pinpoint the exact location of the part of the STN that is to be implanted with a stimulating electrode.

Step 11. The stimulating electrode is implanted in the patient's brain.

choice of filters. The second one is based upon a growing set of filters, where consecutive filters are added according to their rank based upon the area under the receiver operating characteristic (ROC) curve. Additionally, the first, novel approach has also been tested with an SVM classifier with linear and RBF kernels (Duch *et al.*, 2000).

4.1. AdaBoost classification based on predefined sets of filters. In the first approach, classification has been conducted using the AdaBoost classifier with sets predefined (see Definition 14) by the author in Section 3.2. The results of the classification are shown in Table 1.

From Table 1, it can be seen that classification based solely on filters calculated from spike activity yields poor results. It has good sensitivity (0.879), which comes from the fact that the recordings from the STN are characterized by high spiking activity (Israel and Burchiel, 2011). The issue here is that the STN is not the only the area on track of the electrodes that can produce high spiking activity;

Algorithm 2. Classification of recordings for a given electrode e using a set of filters FS and classifier CLS.

Require: data $= \{\text{mer}(e, d) : d \in D\}$
1: results $= \emptyset$
2: **for** $d \in D$ **do**
3: Filter_values $= \emptyset$
4: **for** Filter $\in FS$ **do**
5: $v :=$ Filter(e, d)
6: Filter_values $=$ Filter_values $\cup$ (Filter, v)
7: **end for**
8: $c :=$ CLS(Filter_values)
9: results $=$ results $\cup (d, c)$
10: **end for**
11: **return** results {Returns classes for all recordings}

Table 1. AdaBoost classification results.

Set of filters	Sensitivity	Specificity	ROC area
ALL	0.973	0.961	0.994
DALL	0.971	0.957	0.991
DU2 ∪ DD2	0.969	0.952	0.989
DU1 ∪ DD1	0.955	0.933	0.985
BA ∪ MA	0.948	0.938	0.984
BA	0.934	0.938	0.977
MA	0.948	0.889	0.967
DU1	0.966	0.805	0.913
DU2	0.962	0.801	0.904
DD2	0.911	0.808	0.885
DD1	0.843	0.804	0.878
SA	0.879	0.729	0.856

for example, the SNr—located below the STN—also exhibits slightly different but high spiking. This, in turn, leads to poor specificity (0.729), which—given that recordings taken outside of the STN constitute 83% of all recordings—is not sufficient.

In the case of DD1 or DD2, the results are slightly better than those obtained from spike-derived filters. Filters from those sets can properly distinguish only recordings made below the STN. Classification results obtained using such filters are still better than those based on spikes. This shows how non-specific spike activity can be (Israel and Burchiel, 2011). This can be clearly seen when comparing the mediocre ROC curve obtained for all spike activity-based filters (Fig. 2) with the ROC curve calculated for a single background activity-based filter (Fig. 3).

Results obtained using either DU1 or DU2 are superior because, as explained in Section 3.2, filters from these sets are designed to detect the top border of the STN, i.e., the depth at which the electrode enters the STN. This is why they yield good sensitivity. These filters are, however, unable to discern the bottom border of the STN, and they cannot differentiate recordings from the STN

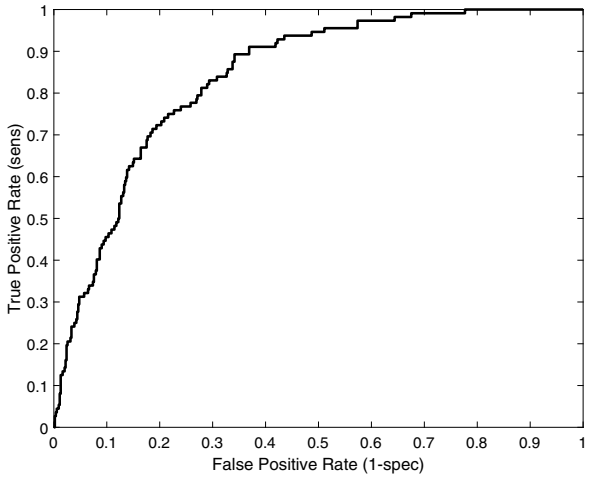

Fig. 2. ROC for spike activity-based filters.

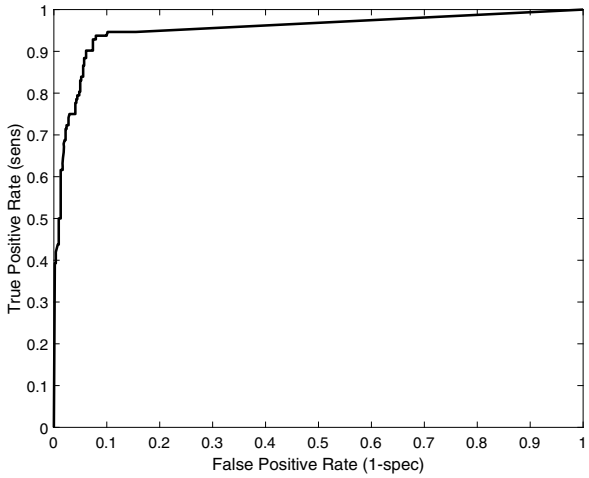

Fig. 3. ROC for PRC80.

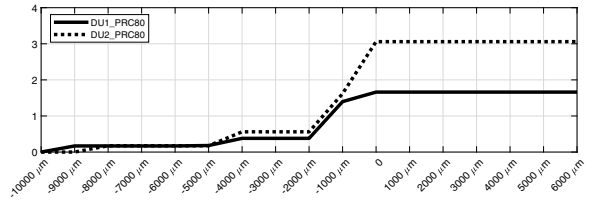

Fig. 4. DU1_PRC80 and DU2_PRC80 values.

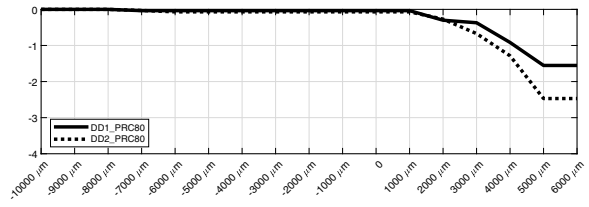

Fig. 5. DD1_PRC80 and DD2_PRC80 values.

from those registered below it. This, in turn, leads to a specificity that is barely above 0.8.

Filters from BA and MA sets are based directly on background noise in the recorded signal. This noise comes from a summation of the activity of neuron cells in the vicinity of the electrode (Israel and Burchiel, 2011). The more neuron cells present in this vicinity, and the more active they are, the louder this noise. Knowing that the STN consists of large amounts of small hyperactive neuron cells (Israel and Burchiel, 2011), these filters provide good sensitivity and specificity. In the case of the BA set, both sensitivity and specificity are above 0.93. The PRC80 filter alone can be used for classification, with a resulting sensitivity of 0.949 and specificity of 0.910. The ROC curve plotted for the first of the folds (for PRC80) is shown in Fig. 3. The problem with these filters is that they show increased values not only for the STN, but also for another structure located below the STN, which may result in false-positive readouts.

Figure 4 shows the DU1_PRC80 and DU2_PRC80 filter values, while Fig. 5 shows the values of the DD1_PRC80 and DD2_PRC80 filters. From both these figures, it becomes clear how the values of the temporal filters act when considered together. Filters DU1_PRC80 and DU2_PRC80 clearly change their values upon entry into the STN, i.e., on its top border, at –1000 μm. Similarly, the DD1_PRC80 and DD2_PRC80 filters signal the point of exit from the STN, i.e., its bottom border, at 4000 μm.

Neither set of filters is able to detect both borders of the STN, but when combined, they should provide good discrimination. Knowing that after the electrodes exit the bottom border of the STN, they very rarely advance much further (Israel and Burchiel, 2011) one might hypothesize that DU1_PRC80 and DU2_PRC80 alone might provide a good basis for discrimination (they distinguish areas above the STN from the STN), while DD1_PRC80 and DD2_PRC80 might not (see Table 1).

This means that the combination of temporal filters might yield very good results. This is indeed the case when considering the DALL set, where the combination yields a sensitivity of 0.971, a specificity of 0.957, and the area under the ROC curve of 0.991. Figure 6 shows the nearly perfect ROC curve obtained for the DALL-filter set.

Table 2 highlights the reasons why the results obtained from the DALL set are better than those obtained from the BA. Here, it becomes evident why the false positive cases for the SNr in BA do not occur in the case of DALL. BA has an elevated value both in the STN and SNr, which, for some patients with more active SNrs, might lead to false-positive detection of the SNr as the STN.

It can be seen from the results of the DU1, DU2, DD1, and DD2 sets that only within the STN, DU1 and DU2 have elevated values, while DD1 and DD2 are

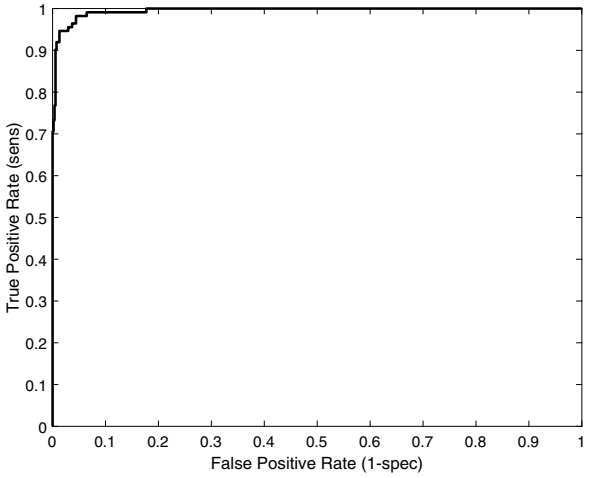

Fig. 6. ROC for the DALL filter set.

Table 2. Expected filter values.

Area	BA	DU1, DU2	DD1, DD2
above the STN	~ 1	~ 0	~ 0
STN	High +	High +	~ 0
below the STN	~ 1	High +	High –
above the SNr	~ 1	High +	High –
SNr	High +	High +	High –

close to zero. Moreover, taking BA, DD1, and DD2 in combination, it becomes clear that the BA is elevated only within the SNr, while DD1 and DD2 are clearly negative.

To remain objective, one must admit that, for some patients, there is no observable space between the STN and SNr (i.e., the space that is below the STN and above SNr) (Israel and Burchiel, 2011; Nieuwenhuys *et al*., 2007). In such cases, false positives might still occur.

Further, it was found that the results obtained with 28 filters were marginally improved. The sensitivity increases by 0.002, the specificity increases by 0.004, and the area under the ROC curve increases by 0.003. Before calculating the DALL set, the BA set also needs to be calculated. To obtain results that are better by a fraction of a per cent, the MA and SA need to be calculated, which is computationally intensive as it contains spike-sorting procedures (Israel and Burchiel, 2011).

4.2. AdaBoost classification based on filters ordered by the ROC area. To obtain verification as to which filters are essential for good classification results, the filters were ranked using Matlab according to their influence on the area under the ROC curve. This value has been calculated for the AdaBoost classifier run with the same parameters as in Section 4.1.

Table 3 and Fig. 7 clearly demonstrate how the classification-quality measures change as subsequent filters are added to the pool used for classification.

The results in Table 3 show how discriminating the filters from the BA set are, especially the PRC80 one. If a maximal simplicity of calculations is the goal, this filter alone gives a sensitivity of 0.949, a specificity of 0.910, and an ROC area of 0.963—all three classification qualities measure above 0.9.

It is also evident that other filters from the BA set follow in importance for classification quality. The first eight rows from the bottom of Table 3 are a steady growth of filters set up to point where all eight filters from BA $\cup$ MA are chosen.

After this point, the DU1 and DU2 sets are added, and then filters based on spike activity. Finally, by adding filters from DD1 and DD2, a full filter set is obtained. As the addition of the remaining nine filters (one from SA, four from DD1, and four from DD2), only improves the value of the area under the ROC curve from 0.993 to 0.994, they were omitted in Table 3 and are referenced in the table as a row with dots.

As this approach adds filters separately, it cannot detect the advantage of the use of, for example, the DU1 and DD1 early. Other filters from other sets, when considered alone, simply give a larger increase in the area under the ROC curve.

4.3. SVM classification based on predefined sets of filters. Not all classification methods are equally suited to any given data. This can be clearly seen in the case of temporal filters, where the effect is very pronounced. One of the most popular and widely used classification methods is SVM (support vector machine) (Williams, 2003). In data science, for some types of data, SVM classifiers are advantageous, while for other types, tree-based ones prove to be superior.

The results provided in Tables 4 and 5 illustrate a case where a tree-based classifier is much better in employing information given by values returned by temporal filters. In the case of the default linear kernel, only filters from the BA set were able to yield sensitivity, specificity, and the area under the ROC curve above 0.9. With the sole exception of DU1 $\cup$ DD1, all results based on temporal filters were poor. In some cases, the sensitivity or specificity was even below 0.4.

The SVM classifier with the RBF kernel, which is often considered superior to the linear one (Apostolidis-Afentoulis and Lioufi, 2015; Jeleń *et al*., 2008) yields temporal filters results that are even worse, as shown in Table 5. In this case, all classifications based solely on temporal filters have the area under the ROC curve below 0.7. In the case of DU1, DD1, DU2, and DD2, the failure of classification is complete; the classifier fails to distinguish the STN recordings and classifies them as recorded outside of the STN (sensitivity

Table 3. Classification results with filters ranked according to the area under the ROC curve.

Set of filters	Sensitivity	Specificity	ROC area
ALL	0.973	0.961	0.994
...	...	...	...
BA ∪ MA ∪ DU1 ∪ DU2 ∪ {AvgSpkRate, AvgSpkRateScMax, BurstRatio}	0.974	0.952	0.993
BA ∪ MA ∪ DU1 ∪ DU2 ∪ {AvgSpkRate, BurstRatio}	0.971	0.957	0.993
BA ∪ MA ∪ DU1 ∪ DU2 ∪ {AvgSpkRate}	0.971	0.955	0.993
BA ∪ MA ∪ DU2 ∪ {DU1_PRC80. DU1_RMS, DU1_HFB, AvgSpkRate}	0.974	0.951	0.992
BA ∪ MA ∪ {DU1_PRC80. DU1_RMS, DU1_HFB, ...			
... DU2_PRC80. DU2_RMS, DU2_HFB, AvgSpkRate}	0.977	0.946	0.992
BA ∪ MA ∪ {DU1_PRC80. DU1_RMS, DU1_HFB, ...			
... DU2_PRC80. DU2_RMS, DU2_HFB}	0.976	0.948	0.992
BA ∪ MA ∪ {DU1_RMS, DU1_HFB, DU2_PRC80. DU2_RMS, DU2_HFB}	0.970	0.951	0.992
BA ∪ MA ∪ {DU1_HFB, DU2_PRC80. DU2_RMS, DU2_HFB}	0.973	0.945	0.991
BA ∪ MA ∪ {DU1_HFB, DU2_RMS, DU2_HFB}	0.973	0.947	0.991
BA ∪ MA ∪ {DU1_HFB, DU2_HFB}	0.964	0.947	0.990
BA ∪ MA ∪ {DU2_HFB}	0.967	0.944	0.989
BA ∪ MA	0.948	0.938	0.984
BA ∪ {MPRC80. MRMS, MHFB}	0.946	0.937	0.984
{PRC80. RMS, HFB, MPRC80. MRMS, MHFB}	0.949	0.928	0.983
{PRC80. RMS, HFB, MPRC80. MRMS}	0.939	0.936	0.981
{PRC80. RMS, HFB, MRMS}	0.942	0.931	0.981
{PRC80. RMS, HFB}	0.947	0.912	0.974
{PRC80. RMS}	0.947	0.912	0.972
{PRC80}	0.949	0.910	0.963

Table 4. SVM classification results: linear kernel.

Set of filters	Sensitivity	Specificity	ROC area
ALL	0.954	0.949	0.987
BA ∪ MA	0.956	0.940	0.985
BA	0.964	0.930	0.984
MA	0.959	0.882	0.972
DU1 ∪ DD1	0.870	0.907	0.909
DU2	0.963	0.767	0.894
DU1	0.961	0.748	0.892
SA	0.906	0.552	0.767
DALL	0.957	0.522	0.697
DU2 ∪ DD2	0.313	0.966	0.569
DD1	0.368	0.785	0.548
DD2	0.621	0.414	0.523

Table 5. SVM classification results: RBF kernel.

Set of filters	Sensitivity	Specificity	ROC area
BA ∪ MA	0.928	0.910	0.957
ALL	0.939	0.838	0.925
MA	0.914	0.787	0.886
BA	0.846	0.785	0.845
SA	0.906	0.552	0.767
DALL	0.957	0.522	0.697
DU1 ∪ DD1	0.933	0.400	0.663
DU2 ∪ DD2	0.313	0.967	0.569
DD1	0.001	1.000	0.508
DU1	0.000	1.000	0.500
DU2	0.000	1.000	0.500
DD2	0.000	1.000	0.500

at or below 0.001, with specificity above 0.999). It is also worth mentioning that the results obtained using the BA ∪ MA set are better than those obtained from the full filter set. The addition of filters based on spike activity or temporal ones has, in fact, worsened the results.

4.4. Classification summary. During the performance evaluation in Section 4, it has been shown that, for the classification of microelectrode data using the filters defined in Section 3.2, the best values of sensitivity, specificity, and the area under the ROC curve can be obtained using the AdaBoost classifier with the author's optimal parameters.

It has been shown that an expert set of 16 temporal filters (DALL) provided by the author can yield optimal results that are comparable to those obtained using all 28 filters. It has also been shown that the automatic selection of the filters by their rank cannot achieve similar performance.

4.5. Performance of selected background activity-based filters. Figure 8 shows the values returned by

the PRC80 filter, calculated for a set of three electrodes (anterior, central, and medial) on the entire track of their recording pass. The recording began at depth, 10000 μm, i.e., 10 mm above the expected location of the STN center and then continued till the bottom border of the STN was passed, and the area below the STN reached a depth of +6000 μm. The location of the STN can be readily identified as the area of an increased filter value. For comparison, in the surgical protocol, the boundaries of the STN have been affixed at -1000 μm to 2000 μm for the central electrode; -1000 μm to 4000 μm for the anterior electrode; and 0 μm to 4000 μm for the medial electrode.

The PRC80 filter has been selected by its ROC rank (Table 3) as the one that is most influential for classification. This filter has been defined by the author in this study. While not being RMS-based, as is the case in most papers in Section 2, it has been found by the ranking method to be superior.

The HFB filter is another filter that merits discussion. This filter is based on frequencies between 500 Hz and 3 kHz. The novelty of this filter comes from the observation that all papers in Section 2 that investigate the power of the signal in certain bands focus only on frequencies below 500 Hz.

The HFB filter also provides additional novel information not found in other filters. Further to showing the top and bottom borders of the STN in a very pronounced way, it often also shows the internal subdivisions of the STN. This can be observed in Fig. 9 at a depth of 1000 μm. The confirmation of the filter importance is shown in Table 3, where this filter is third in the ranking of importance for classification.

Figure 9 shows the HFB filter values as calculated for the same set of three electrodes (anterior, central, and medial) that was used in Fig. 8.

5. Conclusions

The goal of this paper was to provide a set of filters to discriminate recordings registered within the STN from recordings registered outside this brain substructure. The set of filters should contain fewer filters but preserve performance.

Section 3.2 defines various filters that can be used for the discrimination process. Some of them are based on the analysis of the amplitude of the recorded signal, some on the background noise, and finally, some are meta–filters that have been derived from values of other, previously defined filters.

It has been shown in Section 4 that amplitude-based filters, i.e., filters relying on spike detection and sorting, do not provide sufficient discriminating quality. They provide fair sensitivity (0.88); however, they tend to classify recordings from other brain areas (namely, the

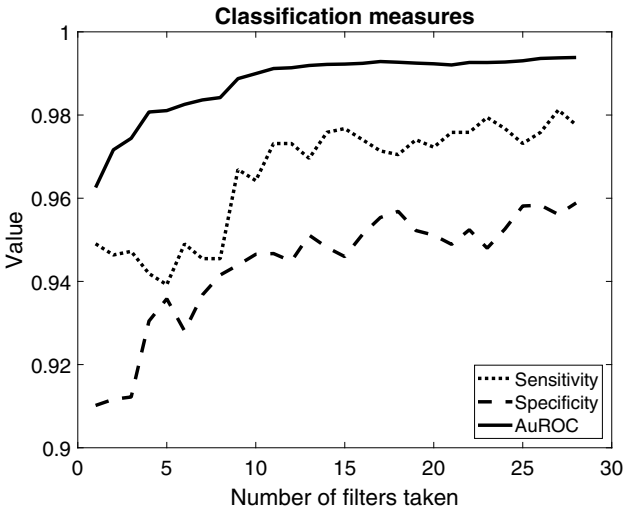

Fig. 7. Changes in the values of classification measures.

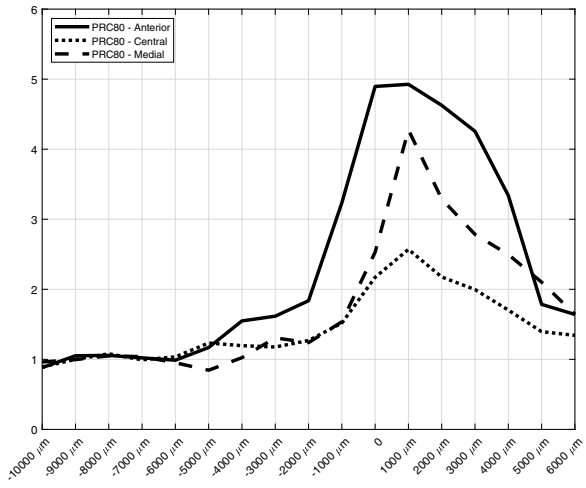

Fig. 8. PRC80 filter values.

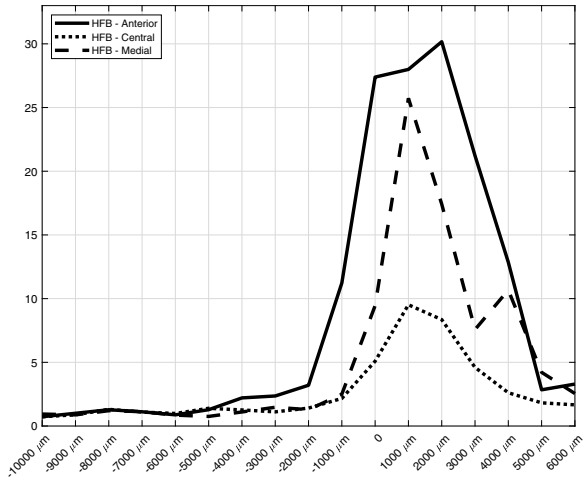

Fig. 9. HFB filter values.

SNr) as the STN and hence are not specific enough (specificity of 0.73).

Background activity-based filters provide much better discriminative power and achieve both sensitivity and specificity above 0.93.

Finally, temporal filters have been fully developed by the author and designed to detect points where electrodes enter and exit the STN (see Section 4.1). They achieved a sensitivity above 0.97 and a specificity above 0.955. The obtained results are all above 0.95 and are competitive with other results from literature.

One of the more interesting findings is that, while temporal filters provide excellent classification results when used with the AdaBoost classifier, they cannot be properly utilized by the SVM.

A further increase in sensitivity, by 0.002, and specificity, by 0.004, can be achieved. However, this requires the calculation of spike activity-based filters, which involves computationally expensive spike sorting, i.e., grouping detected action potentials according to their shape.

For a typical patient, the time required for a full analysis of data from a single hemisphere takes approximately 75 seconds. Additional spike sorting would increase this time by 20 seconds. This can increase the sensitivity and specificity by less than 0.005 for an increase in computing time by over 25%.

A computer system based upon the solution described in this paper can be used in the operation theatre (in real time) during awake brain surgery. Any increase in the processing time automatically increases the duration of the entire surgical procedure. Awake brain surgery is stressful for a patient, and this is the medical and ethical reason to make all necessary calculations as fast as possible.

In this paper, it has been found that using the AdaBoost classifier provides optimal results when a set of 16 filters are used from the DALL set. The calculation of these filters can easily be performed using four filters from the BA set. Calculation of filters from the BA set, while being computationally demanding, cannot be avoided as they provide the discriminative power of the entire solution.

Acknowledgment

The author would like to express his gratitude to Prof. T. Mandat of the Maria Skłodowska-Curie Memorial Oncology Center in Warsaw for sharing his invaluable medical expertise.

References

Anderson, P.B. and Rogers, M.H. (2009). *Deep Brain Stimulation: Applications, Complications and Side Effects*, Nova Biomedical Books, New York, NY.

Apostolidis-Afentoulis, V. and Lioufi, K.I. (2015). SVM classification with linear and RBF kernels, `http://www.academia.edu/13811676/SVM_Classification_with_Linear_and_RBF_kernels`.

Cagnan, H., Dolan, K., He, X., Contarino, M.F., Schuurman, R., Van Den Munckhof, P., Wadman, W.J., Bour, L. and Martens, H.C. (2011). Automatic subthalamic nucleus detection from microelectrode recordings based on noise level and neuronal activity, *Journal of Neural Engineering* **8**(4): 046006.

Ciecierski, K.A., Raś, Z.W. and Przybyszewski, A.W. (2014a). Foundations of automatic system for intrasurgical localization of subthalamic nucleus in Parkinson patients, *Web Intelligence and Agent Systems* **12**(1): 63–82.

Ciecierski, K., Mandat, T., Rola, R., Raś, Z.W. and Przybyszewski, A.W. (2014b). Computer aided subthalamic nucleus (STN) localization during deep brain stimulation (DBS) surgery in Parkinson's patients, *Annales Academiae Medicae Silesiensis* **5**(68): 275–283.

Dietterich, T.G. (2000). Ensemble methods in machine learning, *in* J. Kittler and F. Rodi (Eds), *Multiple Classifier Systems*, Springer, Berlin, pp. 1–15, DOI: 10.1007/3-540-45014-9_1.

Duch, W., Adamczak, R. and Diercksen, G.H.F. (2000). Classification, association and pattern completion using neural similarity based methods, *International Journal of Applied Mathematics and Computer Science* **10**(4): 747–766.

Freeman, E.A. and Moisen, G.G. (2008). A comparison of the performance of threshold criteria for binary classification in terms of predicted prevalence and kappa, *Ecological Modelling* **217**(1–2): 48–58.

Ho, A.L., Ali, R., Connolly, I.D., Henderson, J.M., Dhall, R., Stein, S.C. and Halpern, C.H. (2018). Awake versus asleep deep brain stimulation for Parkinson's disease: A critical comparison and meta-analysis, *Journal of Neurology, Neurosurgery & Psychiatry* **89**(7): 687–691.

Hutchison, W.D., Allan, R.J., Opitz, H., Levy, R., Dostrovsky, J.O., Lang, A.E. and Lozano, A.M. (1998). Neurophysiological identification of the subthalamic nucleus in surgery for Parkinson's disease, *Annals of Neurology* **44**(4): 622–628.

Israel, Z. and Burchiel, K.J. (2011). *Microelectrode Recording in Movement Disorder Surgery*, Thieme, Stuttgart.

Jeleń, Ł., Fevens, T. and Krzyżak, A. (2008). Classification of breast cancer malignancy using cytological images of fine needle aspiration biopsies, *International Journal of Applied Mathematics and Computer Science* **18**(1): 75–83, DOI: 10.2478/v10006-008-0007-x.

Jensen, A. and la Cour-Harbo, A. (2001). *Ripples in Mathematics: The Discrete Wavelet Transform*, Berlin/Heidelberg.

Kano, T., Katayama, Y., Kobayashi, K., Kasai, M., Oshima, H., Fukaya, C. and Yamamoto, T. (2006). Detection of boundaries of subthalamic nucleus by multiple-cell spike density analysis in deep brain stimulation for Parkinson's

disease, *in* J.W. Chang *et al.* (Eds), *Advances in Functional and Reparative Neurosurgery*, Springer, Vienna, pp. 33–35.

Koch, C. (2004). *Biophysics of Computation: Information Processing in Single Neurons*, Oxford University Press, Oxford.

Levy, R., Hutchison, W.D., Lozano, A.M. and Dostrovsky, J.O. (2000). High-frequency synchronization of neuronal activity in the subthalamic nucleus of parkinsonian patients with limb tremor, *Journal of Neuroscience* **20**(20): 7766–7775.

Lewicki, M.S. (1998). A review of methods for spike sorting: The detection and classification of neural action potentials, *Network: Computation in Neural Systems* **9**(4): R53–R78.

Mallet, L., Schüpbach, M., N'Diaye, K., Remy, P., Bardinet, E., Czernecki, V., Welter, M.-L., Pelissolo, A., Ruberg, M., Agid, Y. and Yelnik, J. (2007). Stimulation of subterritories of the subthalamic nucleus reveals its role in the integration of the emotional and motor aspects of behavior, *Proceedings of the National Academy of Sciences* **104**(25): 10661–10666.

Mandat, T.S., Hurwitz, T. and Honey, C.R. (2006). Hypomania as an adverse effect of subthalamic nucleus stimulation: Report of two cases, *Acta Neurochirurgica* **148**(8): 895–898.

Mandat, T., Tykocki, T., Koziara, H., Koziorowski, D., Brodacki, B., Rola, R., Bonicki, W. and Nauman, P. (2011). Subthalamic deep brain stimulation for the treatment of Parkinson disease, *Neurologia i Neurochirurgia Polska* **45**(1): 32–36.

Moran, A., Bar-Gad, I., Bergman, H. and Israel, Z. (2006). Real-time refinement of subthalamic nucleus targeting using Bayesian decision-making on the root mean square measure, *Movement Disorders* **21**(9): 1425–1431.

Nieuwenhuys, R., Voogd, J. and Van Huijzen, C. (2007). *The Human Central Nervous System: A Synopsis and Atlas*, Springer, Berlin.

Novak, P., Daniluk, S., Ellias, S.A. and Nazzaro, J.M. (2007). Detection of the subthalamic nucleus in microelectrographic recordings in Parkinson disease using the high-frequency ($>$ 500 Hz) neuronal background, *Journal of Neurosurgery* **106**(1): 175–179.

Parent, A. and Hazrati, L.-N. (1995). Functional anatomy of the basal ganglia. II: The place of subthalamic nucleus and external pallidium in basal ganglia circuitry, *Brain Research Reviews* **20**(1): 128–154.

Saleh, S., Swanson, K.I., Lake, W.B. and Sillay, K.A. (2015). Awake neurophysiologically guided versus asleep MRI-guided STN DBS for Parkinson disease: A comparison of outcomes using levodopa equivalents, *Stereotactic and Functional Surgeny* **93**(6): 419–426.

Schaltenbrand, G. (1977). *Atlas for Stereotaxy of the Human Brain*, Georg Thieme, Stuttgart.

Schiaffino, L., Muñoz, A.R., Martínez, J.G., Villora, J.F., Gutiérrez, A. and Torres, I.M. (2016). STN area detection using K-NN classifiers for MER recordings in Parkinson patients during neurostimulator implant surgery, *Journal of Physics: Conference Series* **705**(1): 012050.

Shamir, R.R., Zaidel, A., Joskowicz, L., Bergman, H. and Israel, Z. (2012). Microelectrode recording duration and spatial density constraints for automatic targeting of the subthalamic nucleus, *Stereotactic and Functional Neurosurgery* **90**(5): 325–334.

Smith, S.W. (1997). *The Scientist & Engineer's Guide to California Technical*, Digital Signal Processing, Publishing, San Diego, CA.

Temel, Y., Blokland, A., Steinbusch, H.W.M. and Visser-Vandewalle, V. (2005). The functional role of the subthalamic nucleus in cognitive and limbic circuits, *Progress in Neurobiology* **76**(6): 393–413.

Valsky, D., Marmor-Levin, O., Deffains, M., Eitan, R., Blackwell, K. T., Bergman, H. and Israel, Z. (2017). Stop! border ahead: Automatic detection of subthalamic exit during deep brain stimulation surgery, *Movement Disorders* **32**(1): 70–79.

Williams, C.K.I. (2003). Learning with kernels: Support vector machines, regularization, optimization, and beyond, *Journal of the American Statistical Association* **98**(462): 489–489.

Zaidel, A., Spivak, A., Shpigelman, L., Bergman, H. and Israel, Z. (2009). Delimiting subterritories of the human subthalamic nucleus by means of microelectrode recordings and a hidden Markov model, *Movement Disorders* **24**(12): 1785–1793.

Konrad A. Ciecierski received his PhD in computer science from the Warsaw University of Technology, Poland, in 2014. He specializes in the use of machine learning in the fields of medical science, digital signal processing, natural language processing, and deep-learning applications. He is currently an assistant professor and the head of the Bioinformatics and Machine Recognition Department at the NASK Research Institute. He works for the Clinic of Neurosurgery at the Maria Skłodowska-Curie Memorial Oncology Center in Warsaw, where he is a member of the neurosurgical team specializing in the treatment of Parkinson's disease and other movement disorders.

Received: 14 November 2019
Revised: 12 March 2020
Accepted: 29 May 2020